

This is the accepted manuscript made available via CHORUS. The article has been published as:

Suppression of supercollision carrier cooling in high mobility graphene on SiC(0001[over $\bar{1}$])

Takashi Someya, Hirokazu Fukidome, Hiroshi Watanabe, Takashi Yamamoto, Masaru Okada, Hakuto Suzuki, Yu Ogawa, Takushi Iimori, Nobuhisa Ishii, Teruto Kanai, Keiichiro Tashima, Baojie Feng, Susumu Yamamoto, Jiro Itatani, Fumio Komori, Kozo Okazaki, Shik Shin, and Iwao Matsuda

Phys. Rev. B **95**, 165303 — Published 19 April 2017

DOI: [10.1103/PhysRevB.95.165303](https://doi.org/10.1103/PhysRevB.95.165303)

Suppression of supercollision carrier cooling in high mobility graphene on SiC(000 $\bar{1}$)

Takashi Someya,¹ Hirokazu Fukidome,² Hiroshi Watanabe,¹ Takashi Yamamoto,¹ Masaru Okada,¹ Hakuto Suzuki,³ Yu Ogawa,¹ Takushi Iimori,¹ Nobuhisa Ishii,¹ Teruto Kanai,¹ Keiichiro Tashima,² Baojie Feng,¹ Susumu Yamamoto,¹ Jiro Itatani,¹ Fumio Komori,¹ Kozo Okazaki,¹ Shik Shin,¹ and Iwao Matsuda^{1,*}

¹*Institute for Solid State Physics, The University of Tokyo,
Kashiwa-no-ha, Kashiwa, Chiba 277-8581, Japan*

²*Research Institute of Electrical Communication, Tohoku University,
2-1-1 Katahira, Aobaku-ku, Sendai, Miyagi 980-8577, Japan*

³*Department of Physics, School of Science, University of Tokyo,
7-3-1 Hongo, Bunkyo-ku, Tokyo 113-0033, Japan*

(Dated: March 24, 2017)

Graphene, a two-dimensional carbon crystal with a gas of massless Dirac fermions, has promise as a material that is useful in photonic and optoelectronic devices. A comprehensive understanding of carrier cooling in photo-excited graphene is necessary for their applications, however, as competing cooling processes, electron-phonon scattering, and supercollisions, complicates the problem. Specifically, in energy harvesting, supercollision promotes further carrier cooling and, therefore, leads to lower efficiency, placing doubt on the feasibility of device applications. Here we present evidence of suppressed supercollisions in trilayer graphene on a SiC(000 $\bar{1}$) substrate by directly observing photo-excited carriers and numerically analyzing a phenomenological two-temperature model. Knowing that supercollisions restrict the capabilities of graphene-based devices, our results provide a breakthrough for improving their performance.

PACS numbers: 81.05.ue, 78.67.Wj, 78.47.jh, 79.60.-i

I. INTRODUCTION

Because of its broadband absorption, high carrier mobility, and ultrafast optical response, graphene attracts the attention of many researchers as a promising material for next-generation optoelectronic devices. Nowadays, many graphene-based optoelectronic devices are test-manufactured and demonstrated to have a certain practical capability.¹⁻⁹ However, contrary to this fact, the most elementary phenomenon, i.e., dynamics of photo-excited carriers in graphene, is not exactly understood. Therefore, uncovering the carrier dynamics in graphene is essential not only for designing graphene-based optoelectronic devices but also for improving their performance.

Spectroscopic experiments combined with pump-probe techniques, such as time- and angle-resolved photoemission spectroscopy (trARPES),¹⁰⁻¹⁶ transient transmissivity (reflectivity) measurements,¹⁷⁻²² and time-resolved photoluminescence spectroscopy,²³⁻²⁵ have been applied to understand the carrier dynamics in graphene. According to previous research, photo-excited hot carriers lose a large part of their energy via electron-optical phonon scattering within the first several hundred femtoseconds and gradually return to their equilibrium state through electron-acoustic phonon scattering or optical phonon-acoustic phonon decay within 1 to 100 ps.^{17,18} However, although almost all reports agreed with the above scenario; there is no consistency among the decay times reported, implying the existence of extra cooling pathways.

Recently, Song *et al.* predicted a new energy dissipation channel in graphene via disorder-mediated electron-acoustic phonon scatterings, so-called “supercollisions” (SCs).²⁶ A SC takes place through a three-body collision

involving an electron, a defect, and an acoustic phonon. Generally, scattering by an acoustic phonon can transfer much lower energy compared with that by an optical phonon because conservation of momentum for linear dispersion bands restricts the available phase space for scattering and, therefore, acoustic phonon scattering becomes an inefficient cooling channel. However, additional exchanges with disorders enable acoustic phonons to use a much wider phase space, enabling a larger dissipation of energy from the photo-excited carriers. Thus SC becomes an effective cooling pathway. Indeed, SCs have been observed as the dominant cooling channel in a variety of graphene samples, such as suspended²⁷ and substrate-supported^{11,28-30} graphene. As a consequence of these complicated interplays between carriers, optical phonons, acoustic phonons and defects, photo-excited carrier dynamics in graphene has not as yet been clarified.

In our study, we performed trARPES on graphene grown on a SiC(000 $\bar{1}$) C-terminated surface for which the intrinsic carrier mobility exceeded 100,000 cm² V⁻¹ s⁻¹ and experimentally verified suppression of SC cooling processes because of its extremely high carrier mobility. In consequence, we were able to access the intrinsic relaxation process of photo-excited carriers in graphene via electron-optical phonon scattering and optical phonon to acoustic phonon decay processes.

II. EXPERIMENT

The experiments were performed on epitaxial trilayer graphene grown on a SiC(000 $\bar{1}$) substrate. A semi-

insulating 6H-SiC(000 $\bar{1}$) was annealed at 1320 °C for 10 minutes under an Ar atmosphere (1 bar) resulting in epitaxial growth of the trilayer graphene forming on the SiC(000 $\bar{1}$) substrate. After being transferred to an ultra-high vacuum chamber through the air, the sample was cleaned by annealing at 500 °C to remove surface contamination. Low-electron-energy diffraction (LEED) was then used to verify the crystallinity of the cleaned surface. The number of layers, the level of doping ($E_F \sim E_D$), and the stacking structure of the graphene sample were determined from an analysis of ARPES spectra obtained using a He I α source (see Supplemental Material³¹). The intrinsic carrier mobility of the sample is assumed to be 100,000 cm² V⁻¹ s⁻¹. This value was extracted from transport experiments of a top-gated graphene field-effect transistor,³² the graphene sample for which was grown by the same procedures.

The trARPES experiments were performed at a high harmonic generation (HHG) beamline (Institute for Solid State Physics, The University of Tokyo).³³ The laser system comprises a 1-kHz Ti:Sapphire laser operating at a wavelength of 800 nm and pulse width of 70 fs. The HHG laser pulses are generated by irradiating the second harmonic laser pulses in Ar gas and the 9th harmonics with $\hbar\nu = 27.9$ eV were selected by a pair of multilayer mirrors. A series of trARPES spectra were taken with a commercial hemispherical analyzer with a two-dimensional imaging detector (Scienta R4000). Regarding the time-resolved experiments, the 27.9-eV HHG laser pulses were used as light probes and the fundamental laser ($\hbar\nu = 1.55$ eV, 360 – 1650 $\mu\text{J}/\text{cm}^2$) was used as a pump beam. The temporal and energy resolutions were 80 fs and 250 meV, respectively. The delay time of zero (t_0) was defined as a peak intensity of pumping pulse (assumed to be of Gaussian form). Measurements were performed at 20 K and room temperature.

III. RESULTS AND DISCUSSION

Figure 1a–f present a series of trARPES spectra taken at delay times $t = -1.0$ ps, 0 fs, 100 fs, 200 fs, 400 fs, and 1.0 ps, respectively. The graphene sample was excited by 1.55 eV laser (660 $\mu\text{J}/\text{cm}^2$) and the spectra were measured at room temperature. Note that, before irradiation, only the lower Dirac cone is visible (Fig. 1a). Subsequently, after irradiation, the upper Dirac cone appears at the originally unoccupied region.

To highlight pump-induced spectral changes, the spectrum at the equilibrium state (Fig. 1a) is subtracted from the non-equilibrium data (Fig. 1b–f); the differences are displayed in Fig. 1g–k where the scaled red/blue dots indicate the increase/decrease of photoemission intensities compared with that for the equilibrium state.

Figure 2b–e show a comparison of the transient electronic temperatures measured under several pumping fluences; (b) 1650 $\mu\text{J}/\text{cm}^2$, (c) 1100 $\mu\text{J}/\text{cm}^2$, (d) 850 $\mu\text{J}/\text{cm}^2$, and (e) 360 $\mu\text{J}/\text{cm}^2$. The initial temper-

ature was set at 20 K. The electronic temperatures at each delay time were extracted from the angle-integrated energy distribution curves by fitting these curves with the function,^{12,34}

$$I(E, t) = \int D(E') f(E', T_e) G(E - E', \sigma) dE', \quad (1)$$

where $I(E, t)$ is the photoemission intensities at delay time t , $D(E')$ the density of state (DOS) of graphene, $G(E - E', \sigma)$ the Gaussian of width σ as determined by the experimental energy resolution and $f(E', T_e)$ the Fermi–Dirac function at electron temperature T_e . In Figure 2b–e, colored solid dots represent the results of fittings obtained using Eq. 1 (see Supplemental Material³¹). From these fitted results, one can clearly see two distinctive decay regimes in all fluence data: fast (70 fs < t < 800 fs) and slow (t > 800 fs). To understand the underlying relaxation processes, we investigated energetic interchanges between the electronic and phononic systems as well as energy dissipation via SCs.

The optical-phonon modes that contribute to electron-phonon scattering in graphene are the doubly degenerate intravalley E_{2g} modes at the zone center (Γ point) and the intervalley A'_1 mode at the zone corners (K or K' point), whereas all other phonon modes at the Γ and K points contribute negligibly.^{35,36} The corresponding oscillation energies for intravalley E_{2g} and intervalley A'_1 modes are 196 meV and 160 meV, respectively. Regarding electron–optical-phonon scatterings, the carrier recombination (optical-phonon emission) rates (R) and the carrier generation (optical-phonon absorption) rates (G) are given by the following expressions (in units cm⁻²s⁻¹) as proposed by Rana *et al.*,³⁶

$$R = \frac{9}{2} \left(\frac{\partial t}{\partial b} \right)^2 \frac{1}{\pi \rho \omega_{\text{ph}} \hbar^4 v_F^4} \int_{-\infty}^{\infty} dE |E| |E - \hbar \omega_{\text{ph}}| \times f(E, T_e) (1 - f(E - \hbar \omega_{\text{ph}}, T_e)) (1 + n_{\text{ph}}), \quad (2)$$

$$G = \frac{9}{2} \left(\frac{\partial t}{\partial b} \right)^2 \frac{1}{\pi \rho \omega_{\text{ph}} \hbar^4 v_F^4} \int_{-\infty}^{\infty} dE |E| |E + \hbar \omega_{\text{ph}}| \times f(E, T_e) (1 - f(E + \hbar \omega_{\text{ph}}, T_e)) n_{\text{ph}}. \quad (3)$$

Here, $v_F = 1 \times 10^6$ m/s is the Fermi velocity, $\rho = 7.6 \times 10^{-7}$ kg/m² the density. ω_{ph} is the angular frequency for intravalley (196 meV/ \hbar) and intervalley (160 meV/ \hbar) optical-phonon modes and n_{ph} is the phonon population, which follows the Bose–Einstein distribution at the phononic temperature T_{ph} . $\partial t / \partial b$ is related to the change in electronic energy with respect to bond length displacement, where t and b describe the transfer integral and the distance between nearest carbon atoms, respectively. Note that for the values of R and G , the only difference between intravalley and intervalley scattering is the small difference in phonon energies (196 meV for Γ phonon and

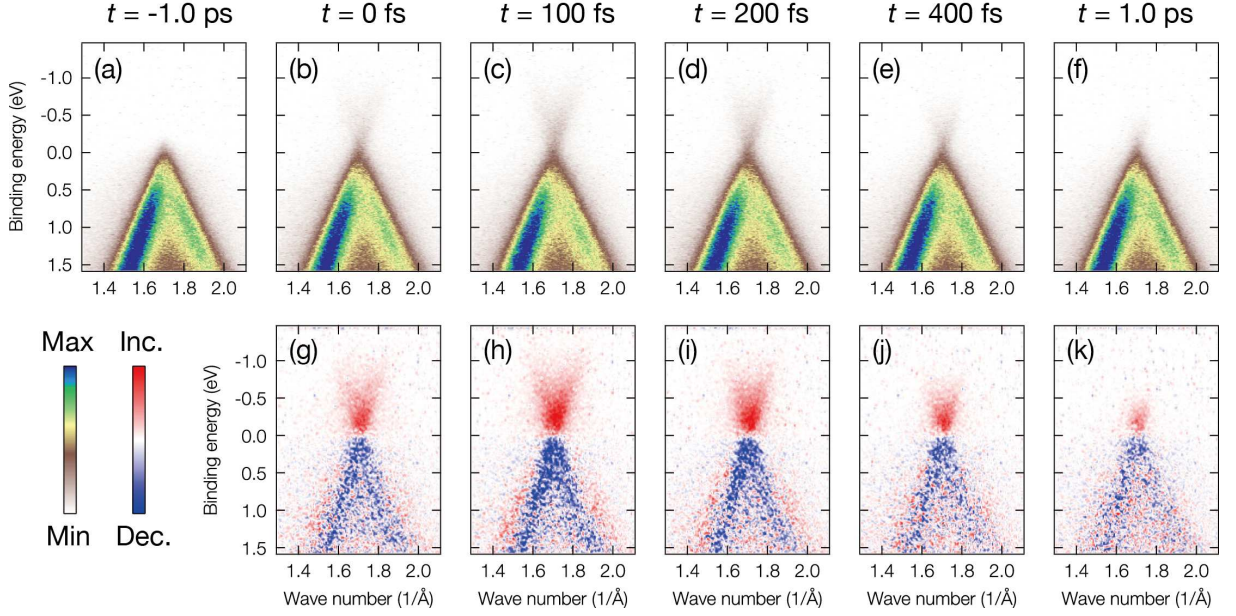


FIG. 1: Temporal evolution of ARPES images taken near the \bar{K} point. (a–f) Series of trARPES spectra taken at specified delay times. The graphene sample was excited by a 1.55-eV pumping laser at $660 \mu\text{J}/\text{cm}^2$. All spectra were measured along the $\bar{\Gamma} - \bar{K} - \bar{M}$ direction of the two-dimensional Brillouin zone and taken at room temperature. (g–k) Difference spectra at the corresponding delay times given in (b–k) obtained by subtracting (a) from each spectrum; the scale red/blue dots indicate increase/decrease from the photoemission intensities at the equilibrium state.

160 meV for K phonon) that gives negligible difference in R and G . Therefore, for simplicity, we consider only Γ phonon mode as a representative for electron–optical-phonon scatterings.

Besides electron–optical-phonon scattering, carrier dynamics can also be affected by SC cooling events. The energy loss rate of SCs, \mathcal{J}_{SC} , depends on the electrical transport properties, such as mean free path, electric conductivity, and carrier mobility.²⁶ The expression for \mathcal{J}_{SC} takes the form

$$\mathcal{J}_{\text{SC}} \sim 8.8 \times 10^{14} \times \frac{D^2}{\mu} (T_e^3 - T_{ac}^3) \left[\frac{\text{eV}}{\text{cm}^2 \text{ K}^3 \text{ s}} \right], \quad (4)$$

where $D \sim 10 - 30 \text{ eV}$ ^{28,37–40} is the deformation potential, μ the intrinsic carrier mobility (with units $\text{cm}^2\text{V}^{-1}\text{s}^{-1}$), T_{ac} the acoustic phonon temperature, which is assumed to be unchanged from the equilibrium state¹¹ (see Supplemental Material³¹ for details of the derivation of Eq. 4).

Taking these factors into account, we built a comprehensive relaxation model for photo-excited carriers in graphene based on phenomenological two-temperature models:^{17,21,22}

$$\frac{dT_e}{dt} = \frac{G_{\text{pump}}}{C_e} - \frac{R^{\text{Net}} \hbar \omega_{\text{ph}}}{C_e} - \frac{\mathcal{J}_{\text{SC}}}{C_e}, \quad (5)$$

$$\frac{dn_{\text{ph}}}{dt} = \frac{R^{\text{Net}}}{M} - \frac{n_{\text{ph}} - n_{\text{ph}}^0}{\tau}. \quad (6)$$

Figure 2a schematically summarizes the energy interactions (transferred energy per unit area and unit time) among above coupled rate equations. Here R^{Net} denotes the total balance between the recombination rate and the generation rate, i.e., the net recombination rate, given by $R^{\text{Net}} = R - G$. M denotes the number of phonon modes that are included in the available phase space for the carrier–phonon scattering. Its magnitude is determined by the energy of the pumping laser E_{pump} expressed as¹⁷ $2 \times [(E_{\text{pump}}/2)/\hbar v_F]^2/4\pi$. G_{pump} represents the energy injected into the sample during laser irradiation and is assumed to be of Gaussian form with a full-width at half-maximum of 70 fs. C_e is the specific heat of the electronic system assumed to be proportional to the square of the electronic temperature;⁴¹ hence, $C_e = \alpha T_e^2$ where α equals $8.14 \times 10^{-17} \text{ J K}^{-3} \text{ cm}^{-2}$ for undoped graphene. n_p^0 is the initial phonon population at 20 K. τ dictates the anharmonic decay process of the optical phonon to the acoustic phonon.⁴² Here G_{pump} , M , $\partial t/\partial b$, and τ are the fitting parameters for these rate equations.

Setting $\mu = 100,000 \text{ cm}^2\text{V}^{-1}\text{s}^{-1}$ and $D = 30 \text{ eV}$, Fig. 2b–e present the fitted results for T_e and T_{ph} for each pumping fluence. Applied fitting parameters except for G_{pump} are almost identical for all fluence data, confirming that the equations 5–6 are valid for describing the carrier dynamics in graphene including its dependence on the pumping fluence (see Supplemental Material³¹ for details of fittings). It is of note that fitted value for $\partial t/\partial b$ (71 eV nm^{-1} per one optical phonon mode) agrees reasonably well with the theoretically calculated

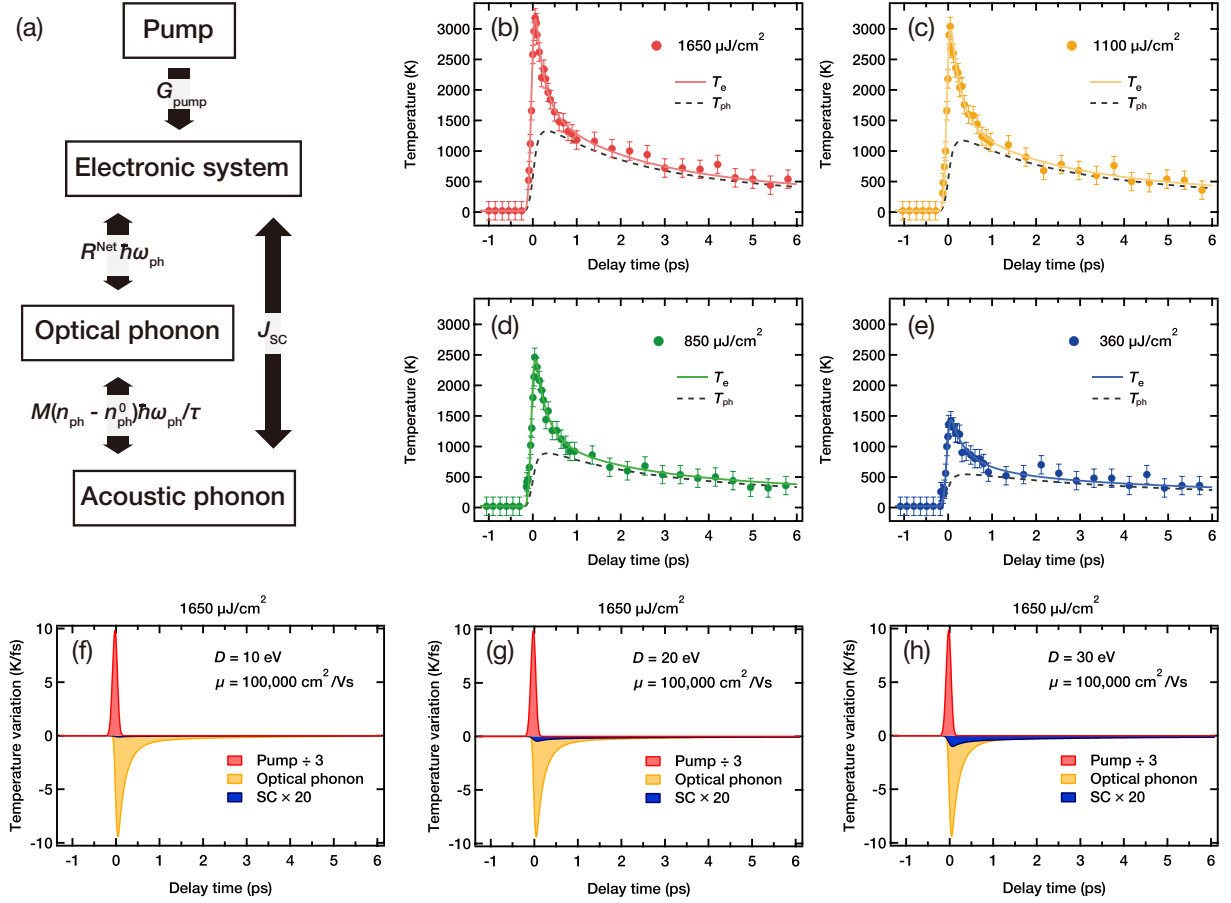


FIG. 2: Temporal variation of the electronic temperatures and the results of the rate equation fittings. (a) Diagrams of the energy interactions between the electronic and phononic systems in graphene based on the rate equations 5–6. (b–e) Comparison of the electronic temperature relaxations under several excitation conditions. Electronic temperatures extracted from Eq. 1 at all delay times are shown in colored solid dots with fitting error bars of ± 100 K. The simulated curves for the transient T_e and T_{ph} at each fluence data were obtained by solving the rate Eqs. 5–6, under the carrier mobility $\mu = 100,000$ cm²/Vs and deformation potential $D = 30$ eV. (f–h) Influence of the SC process on the cooling of the photo-excited carriers in high-mobility graphene within the deformation potential range of 10–30 eV.

value of $\partial t/\partial b = 68$ eV nm⁻¹ for the E_{2g} mode.⁴³ The phonon population n_{ph} is converted to a phononic temperature T_{ph} by inverting the equation for n_{ph} , specifically, $T_{ph} = \hbar\omega_{ph}/k_B \ln[(1 + n_{ph})/n_{ph}]$. Note that the temporal evolution of these temperatures are convolutions with a Gaussian function of width 80 fs (corresponding to the temporal resolution).

Taking Fig. 2b as an example, Fig. 2f–h presents term-by-term comparisons of calculation results for dT_e/dt (right-hand side of Eq. 5); specifically, the heating/cooling rates using the pumping laser, optical phonons and SCs are separately displayed. Comparing the cooling power via SCs (integral of the blue area) with the total cooling power (sum of integral of the yellow and blue areas), SCs contribute with carrier cooling ratio of about 0.1, 0.5, and 1.1 % for deformation potential values of $D = 10, 20$, and 30 eV, respectively, in the measured decay regime (70 fs $< t < 6$ ps). That is, SCs have a negligible influence in decreasing the electronic temperature

in extremely high-mobility graphene.

This is reasonable in terms of mean free path l and scattering time τ_s . Assuming l of the present C-face graphene is ≥ 200 nm, which is the previously reported value of highly oriented pyrolytic graphite (HOPG) with mobility $\mu = 50,000$ cm²V⁻¹s⁻¹,⁴⁴ we obtain $\tau_s \geq 200$ fs using the relation $l = v_F\tau_s$. This time scale is comparable with the fast decay time seen in Fig. 2; that is, SC is expected to happen several times in the fast decay regime. However, for a Si-face graphene, whose mean free path is estimated at 4 nm,¹¹ a much shorter scattering time ($\tau_s = 4$ fs) results in a large energy dissipation via hundreds of SC events. Therefore, as reported in the previous study by Johannsen *et al.*, the observed transient electronic temperature in the Si-face graphene could not be fitted without including the SC term in their rate equations.¹¹ It is worth noting that recent trARPES study by Stange *et al.*⁴⁵ showed that on the carrier cooling in HOPG, not SCs but optical phonon decays de-

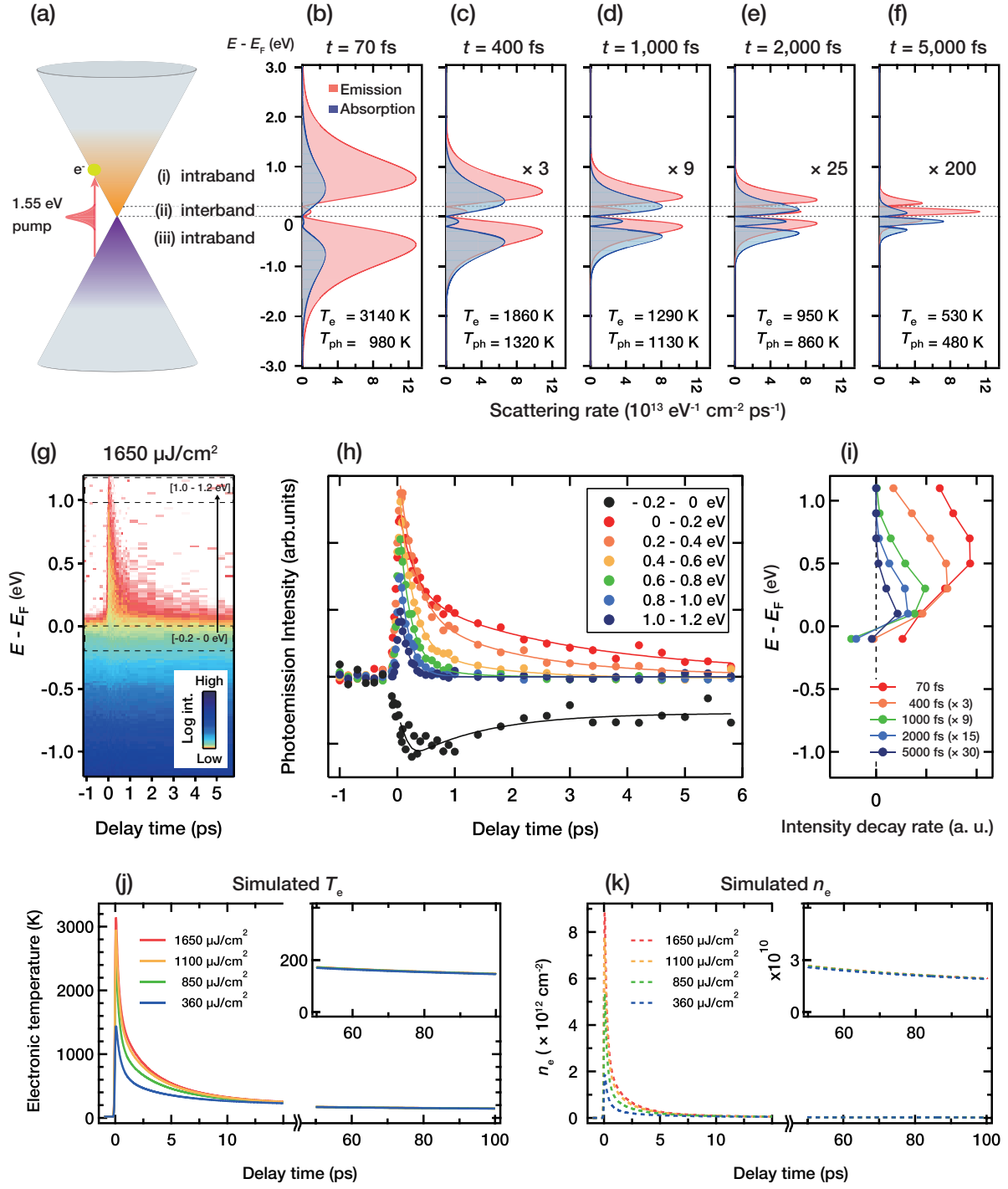


FIG. 3: Simulated rates of intraband- and interband-intravalley scattering as a function of $E - E_F$. (a) Schematic curve for the hot electron distribution has three characteristic energy regimes: electrons at energies below $\hbar\omega_{ph} = 196 \text{ meV}$ step over the conduction band to valence band via optical-phonon emission (labeled (ii) interband) whereas others are scattered within the same band ((i, iii) intraband). (b–f) The energetic distributions of the number of electrons that participate in optical-phonon emission (red) and absorption (blue) per unit time (ps) and unit area (cm^2) are obtained from the integrand of Eqs. (2) and (3), respectively, as a function of $E - E_F$. (g) Transient energy distribution of emitted photoelectrons excited by a 1.55-eV pumping laser at $1650 \mu\text{J}/\text{cm}^2$. (h) Temporal variation of the photoemission intensities (colored circles) collected every 0.2 eV step from -0.2 eV to 1.2 eV, for example, dashed boxes in (g). Colored lines indicate the fitting curves. (i) Photoemission decay rates, i.e., temporal differentiations of (h) at specified delay times are displayed as a function of $E - E_F$. (j, k) Simulated electronic temperatures T_e and carrier densities n_e for several pump conditions are displayed in the long time domain. The insets show enlarged views for delay times of 50–100 ps.

scribe the energy relaxation, closely related to the above scenario and our findings.

From the above discussions, we can now simplify the problem: considering only electron–optical-phonon and optical-phonon–acoustic-phonon scatterings is sufficient for describing the present carrier dynamics. Hence, we investigated further details of the electron–optical-phonon scattering by evaluating the integrands of R and G as a function of $E - E_F$. Figure 3b-f present the simulated emission (absorption) rate of the intravalley E_{2g} optical-phonon modes at each energy level (value of D is set to 30 eV). Regarding optical-phonon emission, three initial electron energy regimes are seen in Fig. 3a: (i) $E - E_F > 196$ meV (intraband scattering), (ii) $196 \text{ meV} > E - E_F > 0$ meV (interband scattering), and (iii) $0 \text{ meV} > E - E_F$ (intraband scattering).

By comparing the number of electrons emitted from each energy regime, we are able to model hot-electron relaxation and to explain what is the cause of the relaxation bottleneck after $t = 800$ fs. At the initial decay regime ($70 \text{ fs} < t < 800 \text{ fs}$), the number of emitted optical phonons (integral of red shaded area) overcomes that of absorbed optical phonons (integral of blue shaded area) (Fig. 3b,c), indicating that the optical-phonon system gains energy from the electronic system, thereby resulting in a rapid rise (fall) in the phononic (electronic) temperature (see Fig. 2b). However, after $t = 800$ fs, the optical-phonon emission and absorption almost equalizes (Fig. 3d-f). Because the net optical phonon emissions decreases, energy transfer between these systems is restrained. For this reason, the relaxation of the electronic temperature is strongly suppressed after $t = 800$ fs. This is also obvious from Fig. 2b-e where the electronic and phononic temperatures almost equalize at $t = 800$ fs. Note that this kind of bottleneck were reported in previous studies^{11,17,18,21,22} and the time scale (~ 800 fs) agree well with these reports.

For comparison with the simulated results, Fig. 3g-i show the experimental results of the energy-resolved decay rate for hot electrons excited at the pumping fluence of $1650 \mu\text{J}/\text{cm}^2$ (corresponding to Fig. 2b). In Fig. 3h, transient photoelectron intensities, $I(t)$, are separately collected from specified energy window; 0.2 eV-step (close to the Γ and K optical phonon energies) from -0.2 eV to 1.2 eV as illustrated by dashed boxes in Fig. 3g. By evaluating intensity decay rate, $dI(t)/dt$, we can obtain the energy distribution of the hot electron decay rates as displayed in Fig. 3i where the decay weight moves from intraband ($t = 70$ fs) to interband ($t = 5000$ fs) scattering regime, showing similar trend to the simulated electron–optical phonon scattering rates (Fig. 3b-f).

Moreover, we note that when the electron distribution approaches the Dirac point, the cooling of the electronic system may be further reduced through bottlenecks arising from the zero DOS at the Dirac point.^{25,46} Specifically, an electron in an initial energy state well above the Dirac point (here we assume $E_D = E_F$) can easily relax to a lower energy state whereas one initially near the Dirac point cannot because the DOS of the final state in the

latter case is much smaller than that in the former case. Therefore, the relaxation of the electronic temperature is significantly restricted when the electron distribution for the Dirac point is approached (for example, see Fig. 3f). Figure 3j and k show the simulated results of the electronic temperatures T_e and carrier densities n_e for the pumping fluence of $360 - 1650 \mu\text{J}/\text{cm}^2$ in the long time domain ($-1 \text{ ps} \sim 100 \text{ ps}$). The results after 6 ps are simulated using fitting parameters obtained from Figs. 2b-e. As seen in the inset of Fig. 3j, T_e has still not relaxed to the initial temperature of 20 K even until 100 ps. This is because a cooling of T_e further stagnates around 5 - 10 ps where the bottleneck effect of the Dirac point may become effective. Indeed, from this point, the electron distribution accumulates near the Dirac point and the interband optical-phonon emission dominates the scattering channel (Fig. 3f). The long time-domain measurement show good agreement with Fig. 3k (see Supplemental Material³¹).

IV. SUMMARY

In summary, we performed trARPES on C-face epitaxial graphene on a SiC(000 $\bar{1}$) substrate. The observed transient electronic temperature consists of fast ($70 \text{ fs} < t < 800 \text{ fs}$) and slow ($t > 800 \text{ fs}$) decay regimes and these features are successfully reproduced by a phenomenological model based on coupled rate equations. Simulations of the time-dependent phonon emission/absorption rate show that slow decay originates from the suppression of energy exchanges between carriers and optical phonons on reaching thermal equilibrium, and also from the suppression of zero carrier DOS near the Dirac point. The influence of SCs on carrier cooling in graphene is assessed. By comparing its effect with competing cooling processes such as optical-phonon scattering, we proved that for high-mobility ($\mu \sim 100,000 \text{ cm}^2 \text{ V}^{-1} \text{ s}^{-1}$) graphene, SCs had little effect on carrier cooling. This indicates that during operations on high-mobility graphene-based devices, energy from light harvesting can be used without added energy losses caused by SCs. As a first demonstration of showing the suppression of SC carrier cooling in graphene, our results provide clear guidelines not only for designing next-generation optoelectronic devices but also for improving their performance.

ACKNOWLEDGEMENTS

This research was supported by the Ministry of Education, Culture, Sports, Science and Technology of Japan (Photon and Quantum Basic Research Coordinated Development Program), a Japan Society for the Promotion of Science grant-in-aid for specially promoting research (#23000008), KAKENHI 16H06361, a NEDO academia-industrial alliance project and by JST, ACT-C.

- * Electronic address: imatsuda@issp.u-tokyo.ac.jp
- ¹ F. Xia, T. Mueller, Y. M. Lin, A. Valdes-Garcia, and P. Avouris, *Nat. Nanotech.* **4**, 839 (2009).
 - ² T. Mueller, F. Xia, and P. Avouris, *Nat. Photonics* **4**, 297 (2010).
 - ³ B. Y. Zhang, T. Liu, B. Meng, X. Li, G. Liang, X. Hu, and Q. J. Wang, *Nat. Commun.* **4**, 1811 (2013).
 - ⁴ V. Ryzhii, V. Mitin, M. Ryzhii, N. Ryabova, and T. Otsuji, *Appl. Phys. Express* **8**, 063002 (2008).
 - ⁵ V. Ryzhii, M. Ryzhii, A. Satou, T. Otsuji, A. A. Dubinov, and V. Y. Aleshkin, *J. Appl. Phys.* **106**, 084507 (2009).
 - ⁶ V. Ryzhii, A. A. Dubinov, T. Otsuji, V. Mitin, and M. S. Shur, *J. Appl. Phys.* **107**, 054505 (2010).
 - ⁷ S. Boubanga-Tombet, S. Chan, T. Watanabe, A. Satou, V. Ryzhii, and T. Otsuji, *Phys. Rev. B* **85**, 035443 (2012).
 - ⁸ T. Watanabe, T. Fukushima, Y. Yabe, S. A. Boubanga Tombet, A. Satou, A. A. Dubinov, V. Ya Aleshkin, V. Mitin, V. Ryzhii, and T. Otsuji, *New J. Phys.* **15**, 075003 (2013).
 - ⁹ M. Liu, X. Yin, E. Ulin-Avila, B. Geng, T. Zentgraf, L. Ju, F. Wang, and X. Zhang, *Nature* **474**, 64 (2011).
 - ¹⁰ I. Gierz, J. C. Petersen, M. Mitrano, C. Cacho, I. C. E. Turcu, E. Springate, A. Stohr, A. Kohler, U. Starke, and A. Cavalleri, *Nat. Mater.* **12**, 1119 (2013).
 - ¹¹ J. C. Johannsen, S. Ulstrup, F. Cilento, A. Crepaldi, M. Zacchigna, C. Cacho, I. C. E. Turcu, E. Springate, F. Fromm, C. Raidel, T. Seyller, F. Parmigiani, M. Grioni, and P. Hofmann, *Phys. Rev. Lett.* **111**, 027403 (2013).
 - ¹² T. Someya, H. Fukidome, Y. Ishida, R. Yoshida, T. Iimori, R. Yukawa, K. Akikubo, Sh. Yamamoto, S. Yamamoto, T. Yamamoto, T. Kanai, K. Funakubo, M. Suemitsu, J. Itatani, F. Komori, S. Shin, and I. Matsuda, *Appl. Phys. Lett.* **104**, 161103 (2014).
 - ¹³ S. Ulstrup, J. C. Johannsen, F. Cilento, J. A. Miwa, A. Crepaldi, M. Zacchigna, C. Cacho, R. Chapman, E. Springate, S. Mammadov, F. Fromm, C. Raidel, T. Seyller, F. Parmigiani, M. Grioni, P. D. C. King, and P. Hofmann, *Phys. Rev. Lett.* **112**, 257401 (2014).
 - ¹⁴ J. C. Johannsen, S. Ulstrup, A. Crepaldi, F. Cilento, M. Zacchigna, J. A. Miwa, C. Cacho, R. T. Chapman, E. Springate, F. Fromm, C. Raidel, T. Seyller, P. D. C. King, F. Parmigiani, M. Grioni, and P. Hofmann, *Nano Lett.* **15**, 326 (2014).
 - ¹⁵ I. Gierz, M. Mitrano, H. Bromberger, C. Cacho, R. Chapman, E. Springate, S. Link, U. Starke, B. Sachs, M. Eckstein, T. O. Wehling, M. I. Katsnelson, A. Lichtenstein, and A. Cavalleri, *Phys. Rev. Lett.* **114**, 125503 (2015).
 - ¹⁶ S. Ulstrup, J. C. Johannsen, A. Crepaldi, F. Cilento, M. Zacchigna, C. Cacho, R. T. Chapman, E. Springate, F. Fromm, C. Raidel, T. Seyller, F. Parmigiani, M. Grioni, and P. Hofmann, *J. Phys.: Condens. Matter* **27**, 164206 (2015).
 - ¹⁷ H. Wang, J. H. Strait, P. A. George, S. Shivaraman, V. B. Shields, M. Chandrashekhara, J. Hwang, F. Rana, M. G. Spencer, C. S. Ruiz-Vargas, and J. Park, *Appl. Phys. Lett.* **96**, 081917 (2010).
 - ¹⁸ J. H. Strait, H. Wang, S. Shivaraman, V. Shields, M. Spencer, and F. Rana, *Nano Lett.* **11**, 4902 (2011).
 - ¹⁹ D. Brida, A. Tomadin, C. Manzoni, Y. J. Kim, A. Lombardo, S. Milana, R. R. Nair, K. S. Novoselov, A. C. Ferrari, G. Cerullo, and M. Polini, *Nat. Commun.* **4**, 1987 (2013).
 - ²⁰ K. J. Tielrooij, J. C. W. Song, S. A. Jensen, A. Centeno, A. Pesquera, A. Z. Elorza, M. Bonn, L. S. Levitov, and F. H. L. Koppens, *Nat. Phys.* **9**, 248 (2013).
 - ²¹ K.-C. Lin, M.-Y. Li, L. J. Li, D. C. Ling, C. C. Chi, and J.-C. Chen, *J. Appl. Phys.* **113**, 133511 (2013).
 - ²² K.-C. Lin, M.-Y. Li, D. C. Ling, C. C. Chi, and J.-C. Chen, *Phys. Rev. B* **91**, 125440 (2015).
 - ²³ C. H. Lui, K. F. Mak, J. Shan, and T. F. Heinz, *Phys. Rev. Lett.* **105**, 127404 (2010).
 - ²⁴ W.-T. Liu, S. W. Wu, P. J. Schuck, M. Salmeron, Y. R. Shen, and F. Wang, *Phys. Rev. B* **82**, 081408 (2010).
 - ²⁵ H. Watanabe, T. Kawasaki, T. Iimori, F. Komori, and T. Suemoto, *Chem. Phys. Lett.* **637**, 58 (2015).
 - ²⁶ J. C. W. Song, M. Y. Reizer, and L. S. Levitov, *Phys. Rev. Lett.* **109**, 106602 (2012).
 - ²⁷ A. Laitinen, M. Oksanen, A. Fay, D. Cox, M. Tomi, P. Virtanen, and P. J. Hakonen, *Nano Lett.* **14**, 3009 (2014).
 - ²⁸ T. V. Alencar, M. G. Silva, L. M. Malard, and A. M. de Paula, *Nano Lett.* **14**, 5621 (2014).
 - ²⁹ M. W. Graham, S.-F. Shi, D. C. Ralph, J. Park, and P. L. McEuen, *Nat. Phys.* **9**, 103 (2013).
 - ³⁰ A. C. Betz, S. H. Jhang, E. Pallecchi, R. Ferreira, G. Fève, J. M. Berroir, and B. Plaças, *Nat. Phys.* **9**, 109 (2013).
 - ³¹ See Supplemental Material at [URL will be inserted by publisher] for the sample characterization, derivation of Eq. 4, details of the fitting parameters, and long delay data.
 - ³² A. Satou, G. Tamamushi, K. Sugawara, J. Mitsushio, V. Ryzhii, and T. Otsuji, *IEEE Trans. Electron Devices*, **63**, 3300 (2016).
 - ³³ K. Ishizaka, T. Kiss, T. Yamamoto, Y. Ishida, T. Saitoh, M. Matsunami, R. Eguchi, T. Ohtsuki, A. Kosuge, T. Kanai, M. Nohara, H. Takagi, S. Watanabe, and S. Shin, *Phys. Rev. B* **83**, 081104 (2011).
 - ³⁴ Y. Ishida, T. Togashi, K. Yamamoto, M. Tanaka, T. Taniuchi, T. Kiss, M. Nakajima, T. Suemoto, and S. Shin, *Sci. rep.* **1**, 64 (2011).
 - ³⁵ S. Piscanec, M. Lazzeri, F. Mauri, A. C. Ferrari, and J. Robertson, *Phys. Rev. Lett.*, **93**, 185503 (2004).
 - ³⁶ F. Rana, P. A. George, J. H. Strait, J. M. Dawlaty, S. Shivaraman, M. Chandrashekhara, and M. G. Spencer, *Phys. Rev. B* **79**, 115447 (2009).
 - ³⁷ K. Sugihara, *Phys. Rev. B* **28**, 2157 (1983).
 - ³⁸ K. I. Bolotin, K. J. Sikes, J. Hone, H. L. Stormer, and P. Kim, *Phys. Rev. Lett.* **101**, 096802 (2008).
 - ³⁹ D. K. Efetov, and P. Kim, *Phys. Rev. Lett.* **105**, 256805 (2010).
 - ⁴⁰ C. R. Dean, A. F. Young, I. Meric, C. Lee, L. Wang, S. Sorgenfrei, K. Watanabe, T. Taniguchi, P. Kim, K. L. Shepard, and J. Hone, *Nat. Nanotech.* **5**, 722 (2010).
 - ⁴¹ D. Sun, C. Divin, C. Berger, W. A. de Heer, P. N. First, and T. B. Norris, *Phys. Status Solidi C* **8**, 1194 (2011).
 - ⁴² N. Bonini, M. Lazzeri, N. Marzari, and F. Mauri, *Phys. Rev. Lett.* **99**, 176802 (2007).
 - ⁴³ S. Pisana, M. Lazzeri, C. Casiraghi, K. S. Novoselov, A. K. Geim, A. C. Ferrari, and F. Mauri, *Nature Mater.* **6**, 198 (2007).
 - ⁴⁴ N. García, P. Esquinazi, J. Barzola-Ququia, B. Ming, and D. Spodig, *Phys. Rev. B* **78**, 035413 (2008).
 - ⁴⁵ A. Stange, C. Sohr, L. X. Yang, G. Rohde, K. Janssen, P.

Hein, L.-P. Oloff, K. Hanff, K. Rossnagel, and M. Bauer, Phys. Rev. B **92**, 184303 (2015).

⁴⁶ S. Butscher, F. Milde, M. Hirtschulz, E. Malić, and A.

Knorr, Appl. Phys. Lett. **91**, 203103 (2007).